

Aseismic Slip and Cascade Triggering Process of Foreshocks Leading to the 2021 M_w 6.1 Yangbi Earthquake

Xiaoge Liu¹ , Wenbin Xu^{*1} , Zilong He¹, Lihua Fang², and Zhidan Chen¹

Abstract

Understanding the nature of foreshock evolution is important for earthquake nucleation and hazard evaluation. Aseismic slip and cascade triggering processes are considered to be two end-member precursors in earthquake nucleation processes. However, to perceive the physical mechanisms of these precursors leading to the occurrence of large events is challenging. In this study, the relocated 2021 Yangbi earthquake sequences are observed to be aligned along the northwest-southeast direction and exhibit spatial migration fronts toward the hypocenters of large events including the mainshock. An apparent static Coulomb stress increase on the mainshock hypocenter was detected, owing to the precursors. This suggests that the foreshocks are manifestations of aseismic transients that promote the cascade triggering of both the foreshocks and the eventual mainshock. By jointly inverting both Interferometric Synthetic Aperture Radar and Global Navigation Satellite Systems data, we observe that the mainshock ruptured a blind vertical fault with a peak slip of 0.8 m. Our results demonstrate that the lateral crustal extrusion and lower crustal flow are probably the major driving mechanisms of mainshock. In addition, the potential seismic hazards on the Weixi-Weishan and Red River faults deserve further attention.

Cite this article as Liu, X., W. Xu, Z. He, L. Fang, and Z. Chen (2022). Aseismic Slip and Cascade Triggering Process of Foreshocks Leading to the 2021 M_w 6.1 Yangbi Earthquake, *Seismol. Res. Lett.* **XX**, 1–16, doi: 10.1785/0220210263.

Supplemental Material

Introduction

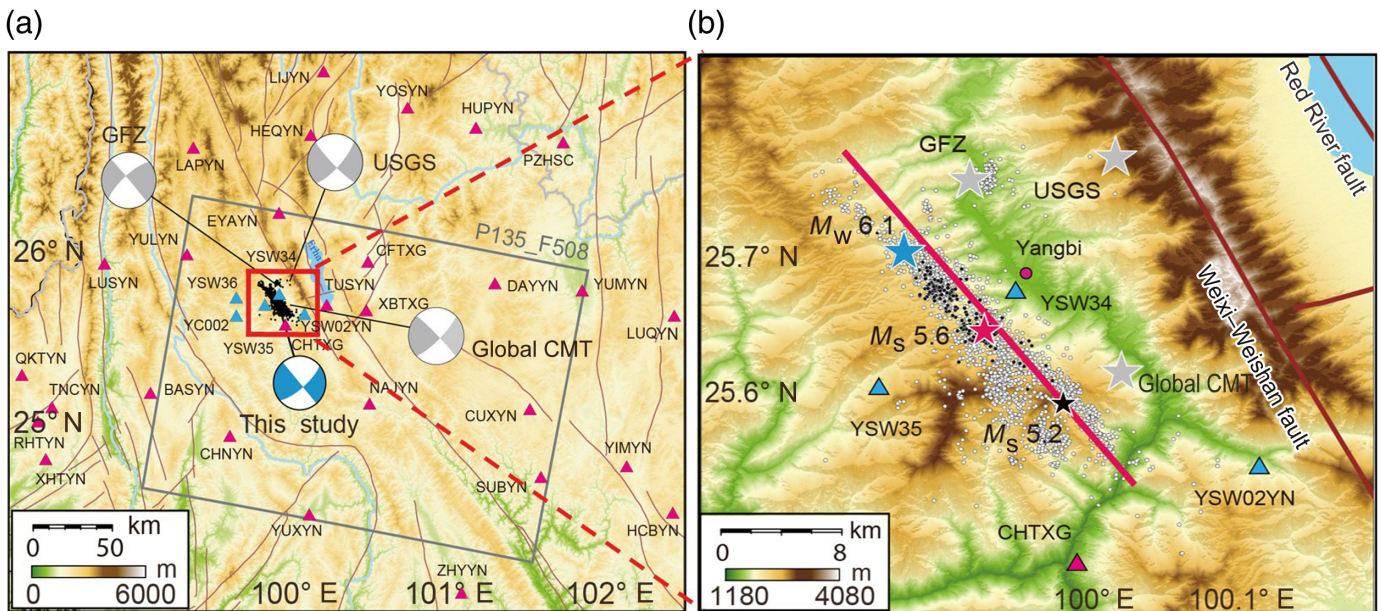
The physical processes that lead to large earthquakes remain a fundamental unresolved scientific question with significant societal and economic importance (Kato and Ben-Zion, 2021). Foreshocks preceding mainshock are common precursors and indicated to be the most informative signals for the nucleation processes of large earthquakes (Ross *et al.*, 2020). Two classic end-member conceptual models, the aseismic slip model (Dodge *et al.*, 1996) and cascade triggering model (Beroza and Ellsworth, 1996) have been proposed to address the nucleation processes. In the aseismic slip model, earthquakes are triggered by aseismic slip over an extended area near the eventual mainshock hypocenter, which might be the precursor signals for the mainshock. In the cascade triggering model, earthquakes are triggered by stress transfer between one foreshock and another without aseismic slip (Ellsworth and Bulut, 2018), which indicates random earthquake occurrence. However, the triggering roles of aseismic slip and/or cascade stress transfer during earthquake nucleation remain debatable. Bouchon *et al.* (2011) proposed that the repetitive foreshocks before the 1999 M_w 7.6 Izmit earthquake were due to aseismic slip, based on waveform similarity. Ellsworth and Bulut (2018) inferred that one foreshock loads the adjacent one, causing its failure. This failure was studied based on

the static stress change calculation, indicating cascade triggering of the Izmit mainshock. Based on the spatiotemporal migration of the foreshock sequence, the lower average stress drops, and the depletion of high-frequency energy; Chen and Shearer (2013) suggested that California foreshock sequences (1992 M_w 7.3 Landers, 1999 M_w 7.1 Hector Mine, and 2010 M_w 7.2 El Mayor-Cucapah) are manifestations of aseismic slip. Yoon *et al.* (2019) argued that the 1999 Hector Mine foreshocks and mainshock are triggered by cascade stress transfer based on little source radius overlap and the increase in shear stress on the hypocenter of later event from its foreshock. Kato *et al.* (2012) indicated that propagation of slow slip led to the 2011 M_w 9.0 Tohoku earthquake, based on the repeating earthquakes and the migrating seismicity to the mainshock hypocenter. In contrast, Marsan and Enescu (2012) proposed that aseismic slip is not required to elucidate the whole sequence by modeling the foreshock sequence, indicating

1. Laboratory of Volcano and Earthquake Research, School of Geosciences and Info-Physics, Central South University, Changsha, Hunan, People's Republic of China,  <https://orcid.org/0000-0002-5762-5218> (XL);  <https://orcid.org/0000-0001-7294-8229> (WX); 2. Institute of Geophysics, China Earthquake Administration, Beijing, China

*Corresponding author: wenbin.xu@csu.edu.cn

© Seismological Society of America



the dominance of the cascade triggering model in the mega-thrust earthquake nucleation process. Recently, the combined effects of aseismic slip and cascade triggering on the evolution of earthquake sequences were analyzed in the 2010 M_w 7.2 El Mayor–Cucapah earthquake based on the spatiotemporal evolution and source parameters of foreshocks (Yao *et al.*, 2020), and in the 2016 M_w 7.0 Kumamoto earthquake based on the migrations of seismicity fronts and Coulomb stress change (Kato *et al.*, 2016). The combined contributions of the two end-member models were confirmed by laboratory observations (McLaskey and Lockner, 2014; Yamashita *et al.*, 2021), which indicates the relative contributions of aseismic slip and cascade triggering on the nucleation process, controlled by fault heterogeneity.

The M_w 6.1 Yangbi earthquake occurred at the western boundary of the Sichuan-Yunnan block in the southeastern Tibetan plateau on 21 May 2021 (Fig. 1). The complex tectonic deformations in the region are characterized by large-scale eastward extrusion of the plateau materials and the clockwise rotation around the eastern Himalayan syntaxis (Wang and Shen, 2020). Previous studies exhibited that the Yangbi earthquake sequence is a typical foreshock–mainshock–aftershock sequence (Long *et al.*, 2021; Su *et al.*, 2021; Zhang *et al.*, 2022). The mainshock was preceded and followed by an intense earthquake sequence that had initiated three days prior to the mainshock; this included an M_s 5.6 foreshock that occurred approximately 27 min in advance (Fig. 1). The field investigation indicated no evident surface rupture, except for a ~5 km long minor surface fracture (Li *et al.*, 2021). In addition, it was found that the seismogenic fault of the Yangbi earthquake is a northwest-trending secondary fault on the western side of the Weixi–Weishan fault. In several studies, this secondary fault is illuminated by the relocation earthquake sequence (Long *et al.*, 2021; Su *et al.*, 2021; Yang *et al.*, 2021). The focal

Figure 1. Tectonic map of the study area. (a) The gray rectangle represents the coverage of the Synthetic Aperture Radar (SAR) image. The purple and gray focal mechanism plots represent the focal mechanism solutions from our geodetic inversion results and other institutions, respectively. The brown lines represent the regional faults. (b) An enlarged view of the red rectangular area in (a). The black and white dots represent the relocated foreshocks and aftershocks. The blue, red, and black stars represent relocated locations of mainshock (M_w 6.1), largest foreshock (M_s 5.6), and largest aftershock (M_s 5.2), respectively. The color version of this figure is available only in the electronic edition.

mechanism and seismic waveform inversion studies revealed that the Yangbi earthquake is dominated by dextral strike slip along with a minor normal slip component (Long *et al.*, 2021; Su *et al.*, 2021; Yang *et al.*, 2021). This is in accordance with the inverted fault-slip distribution based on the Global Navigation Satellite Systems (GNSS) and/or Interferometric Synthetic Aperture Radar (InSAR) (Wang *et al.*, 2021; Zhang, Gan, *et al.*, 2021). The existing research mostly focuses on identifying seismogenic faults, inverting slip distributions, and relocating earthquake sequences. However, there is still bitter dispute on the mechanisms driving the foreshock sequence of the 2021 Yangbi earthquake. Some studies have proposed diverse mechanisms for the foreshock sequence (e.g., cascade triggering [Yang *et al.*, 2021; Zhang *et al.*, 2022] and fluid flow [Lei *et al.*, 2021; Su *et al.*, 2021]). Thus, it is important to further investigate and analyze the nucleation-related spatiotemporal evolution and stress transfer of foreshocks and aftershocks in relation to the Yangbi earthquake, which is significant for an improved understanding of the nucleation process.

In this study, we utilize the double-difference method to relocate the Yangbi earthquake sequence for a detailed investigation of the spatiotemporal seismicity evolution (Waldhauser and

Ellsworth, 2000) and nucleation processes of the earthquake sequence. Furthermore, we use InSAR and GNSS data to generate the coseismic displacement field, which is used to invert the source parameters, based on the Bayesian method (Bagnardi and Hooper, 2018). In addition, we invert the temporal regional maximum principal stress in the region to analyze the possible driving mechanisms. Finally, we implement the Coulomb stress calculation to relate the aftershock distribution and evaluate the regional seismic hazards.

Data and Methods

Seismicity relocation

Seismicity relocation requires accurate S- and P-wave differential travel times, which are related to the number of seismic stations. There are more than 100 well-covered permanent and temporary stations in the Yangbi earthquake region, including 14 (or 4) seismic stations within a radius of 100 (or 10) km from the epicenter region. These dense seismic stations make the Yangbi earthquake the best one of that recorded by the Chinese Seismic Networks. To avoid weakly linked pairs and obtain reliable results, we selected 2153 earthquakes with a maximum gap angle $\leq 180^\circ$ and phase number ≥ 10 , spanning from 18 to 28 May 2021, from the initial 3545 earthquakes ($M_s = -1.8$ to 6.4) reported by the Yunnan seismic network. The double-difference relative location method was adopted to relocate the 2021 seismic event sequence (Waldhauser and Ellsworth, 2000). After composing the earthquake pairs based on the initial source locations, we selected a group of adjacent phases. The S- and P-wave differential travel times were calculated and utilized to estimate earthquake sequence locations. Using 19,090 S-wave and 25,271 P-wave differential travel-time observations, a total number of 2144 earthquakes were relocated with average location errors of the east–west (0.21 km), north–south (0.29 km), and vertical directions (0.29 km). Based on similar seismic stations (Fig. 1), Zhang et al. (2022) found that the horizontal and vertical location uncertainties is about 400 and 2000 m using the bootstrapping method, respectively. In addition, the smallest magnitude ($M_s = -1.4$) and all small magnitude ($M_s \leq -0.4$) of relocated events occurred after the mainshock, which is attributed to several temporary stations near the hypocenter region after the mainshock (Fig. 1).

InSAR and GNSS data processing

GAMMA software was utilized to process the primary and secondary Sentinel-1A descending images acquired on 10 and 22 May 2021, respectively, to map the coseismic displacement (Wegmüller et al., 2016). Because of the terrain observation by progressive scan imaging mode of the Sentinel-1 data, the spectral diversity method was applied to the primary and secondary images after initial rough registration (Prats-Iraola et al., 2012). Furthermore, a 10×2 multilooking operation was performed to reduce noise and a 30 m Shuttle Radar

Topography Mission digital elevation model was utilized to simulate and remove the topographic phase (Farr et al., 2007). To further improve the signal-to-noise ratio, an improved power spectrum filter was applied to the interferogram (Li et al., 2008). Further, the phase unwrapping process was completed utilizing the minimum cost flow method (Chen and Zebker, 2002). We implemented a novel atmosphere correction method (Cao et al., 2021) to interpolate the atmospheric parameters of the ERA5 (see Data and Resources) reanalysis data and generate the atmospheric delay of the interferogram. After subtracting the atmospheric delay, we masked the deformed area and removed the ramp trend. Zhang, Gan, et al. (2021) used the GIPSY-OASIS software to process 37 GNSS data points in PPP mode within 50 km of Eryuan County. As the far-field GNSS data do not exhibit pronounced displacement, we solely adopted the four nearest GNSS sites namely, YBZZ, YBXL, H204, and YBZM in the inversion of fault parameters.

Bayesian coseismic slip distribution inversion

Based on the elastic half-space rectangular dislocation model (Okada, 1985), the position, geometry, and slip distribution of the fault plane can be inverted using geodetic observations. In this study, we followed a two-step inversion strategy for inversion (Xu, 2017). First, the fault geometry was determined through nonlinear inversion, utilizing the Geodetic Bayesian Inversion Software (GBIS) (Bagnardi and Hooper, 2018). The GBIS software adopts the Monte Carlo method to obtain the posterior probability distribution of the parameters. The posterior probability is expressed as follows:

$$p(m|d) = \frac{p(d|m)p(m)}{p(d)}. \quad (1)$$

Among them, $p(d|m)$ is the likelihood function determined by the model parameter m and the observation value d . In equation (1), $p(m)$ represents the prior probability distribution of the model parameter and $p(d)$ is an arbitrary constant. For each iteration, Green's function G is recalculated and the likelihood function is updated. The calculation formula is as follows:

$$p(d|m) = (2\pi)^{-N/2} \left| \sum_d \right|^{-\frac{1}{2}} \times \exp \left[-\frac{1}{2} (d - Gm)^T \sum_d^{-1} (d - Gm) \right], \quad (2)$$

in which N is the number of observations and \sum_d^{-1} is the inverse matrix of the variance-covariance. We obtained the optimal fault parameters through one million sampling operations (Table S2, available in the supplemental material to this article).

Furthermore, we fixed the strike $319.7^{\circ}_{-0.48}^{+0.89}$ and dip $89.8^{\circ}_{-1.2}^{+0.003}$ of the fault, extended the fault to a 30 km length and 15 km width, discretized the fault plane into $2.5 \text{ km} \times 2.5 \text{ km}$ small patches, and obtained the distributed fault-slip

model through the linear inversion with the Bayesian regularized inversion (Amey *et al.*, 2018). This method updates the likelihood function with a similar iterative scheme as the GBIS. During the inversion process, the rake angle was confined from -150° to -190° . After tens of millions of iterations, the slip distribution with the maximum-likelihood value was obtained. To reduce the redundancy of InSAR observations, we utilized the quadtree method to downsample the InSAR data, which resulted in 1947 high-quality points. Furthermore, the exponential model was utilized to model the spatially correlated error (Bagnardi and Hooper, 2018) and construct the variance–covariance matrix, which was utilized to weight the InSAR data during the inversion. For simplicity, we weighted the InSAR and GNSS data equally.

Focal mechanism and stress inversion

To probe the temporal stress fields in the 2021 Yangbi earthquake region, a database of focal mechanisms was compiled including 35 solutions (Hu, 2020), and 64 solutions reported by the EarthX reporting system (see [Data and Resources](#)). The dataset covers a total of 99 focal mechanism solutions with $M_s \geq 3.3$ and spans the 1970–2021 time interval (Table S3). An iterative joint inversion method (Vavryčuk, 2014) was adopted to calculate the triaxial stress field $\sigma_1, \sigma_2, \sigma_3$, and stress shape ratio $R = (\sigma_1 - \sigma_2)/(\sigma_1 - \sigma_3)$, $0 \leq R \leq 1$. Here, $\sigma_1 > \sigma_2 > \sigma_3$ is under the positive compression stress convention and R describes the relative magnitudes of the principal compressive stresses (Warren-Smith *et al.*, 2019). No prior information is required regarding existing tectonic faults due to the fault instability algorithm nested in the iterative joint inversion method (Lund and Slunga, 1999). In addition, this method enables quantification of the confidence intervals of optimal parameters by a bootstrap resampling approach (Michael, 1987), in which each nodal plane can be selected with equal probability in the bootstrap sampling. We estimated 2000 bootstrap samples by adding a random noise of 10° and evaluated 95% confidence region of the optimal stress parameters in the Yangbi earthquake region. The average misfit angle α , which describes the difference between the observed and predicted fault-slip directions, can be utilized to evaluate the success of the stress inversion.

Results

Seismicity relocation results

The locations of the precisely relocated seismicity that occurred three days prior to and seven days after the 2021 $M_w 6.1$ Yangbi earthquake are displayed in Figure 2. Overall, these foreshocks and aftershocks are distributed in the northwest–southeast direction, which is in accordance with the results reported in previous studies (Long *et al.*, 2021; Su *et al.*, 2021). On 18 May, the seismic activity gradually approached the depth of the mainshock. However, it was concentrated in an extremely local region and did not propagate to the mainshock hypocenter. In addition, the foreshocks

initiated at the hypocenter of the largest M_s 5.6 foreshock (Fig. 2). On 19 May, the seismic activity demonstrated evident characteristics of approaching the mainshock hypocenter with a seismic gap during the daytime (8 a.m.–8 p.m.). Although the seismic activity propagated to the hypocenter of the mainshock, it did not trigger the mainshock immediately, indicating that the stress conditions at the mainshock initiation point did not reach the critical yield strength. The seismic activity observed from 18 to 20 May, occurred between the mainshock and the largest foreshock (Fig. 2). The continuous accumulation of stress perturbation induced by nucleation processes (aseismic slip and/or cascade triggering) was likely large enough to trigger the largest M_s 5.6 foreshock, which likely promoted fault failure of the mainshock. On 21 May, most foreshocks occurred until the largest foreshock occurred 27 min before the mainshock. After the mainshock occurred, the aftershocks appeared in clusters and rapidly propagated to the southeast direction. On the second day after the earthquake a local seismic cluster activity appeared in the northeast of the mainshock, which may reflect the disturbance of coseismic stress on the surrounding secondary faults.

Coseismic displacements, fault parameters, and slip distribution

The coseismic displacement field is characterized by a double-lobe pattern with a peak line of sight (LoS) displacement of approximately 9 cm (Fig. 3a). The northeastern and southwestern lobes were characterized by a decrease and an increase in the LoS range, respectively. This indicates the dominant dextral right-lateral fault slip occurred during the mainshock and is consistent with the tectonic setting and focal mechanism solutions (Long *et al.*, 2021; Yang *et al.*, 2021). The ground deformation pattern is almost symmetrical, which suggested a relatively vertical fault dip angle. No evident fractures in the InSAR coseismic displacement suggest buried slip; this indicates a possible shallow slip deficit. The deformation signal at the northwest corner of the epicenter exhibited a diffuse characteristic, which may be partially caused by the foreshocks or aftershocks, especially from the two large foreshocks ($M_s > 5$) that occurred during the image acquisition period. The GNSS horizontal displacements are in accordance with the characteristics of the dextral strike-slip event. The GNSS horizontal displacements are greater near the epicenter, and the maximum horizontal deformation is approximately 4.6 cm at H204. The deformations at other GNSS sites are 4 cm at YBZZ, 3.4 cm at YBXL, and 3 cm at YBZM.

The fault parameters obtained in this study are similar to the Global Centroid Moment Tensor solution, indicating the occurrence of the earthquake on an approximately vertical fault (Table S1). The posterior possibility distribution demonstrates that the fault is well constrained by the geodetic observations, although the trade-off between length, dip angle, and the strike-slip component can be observed (Fig. 4a). The main

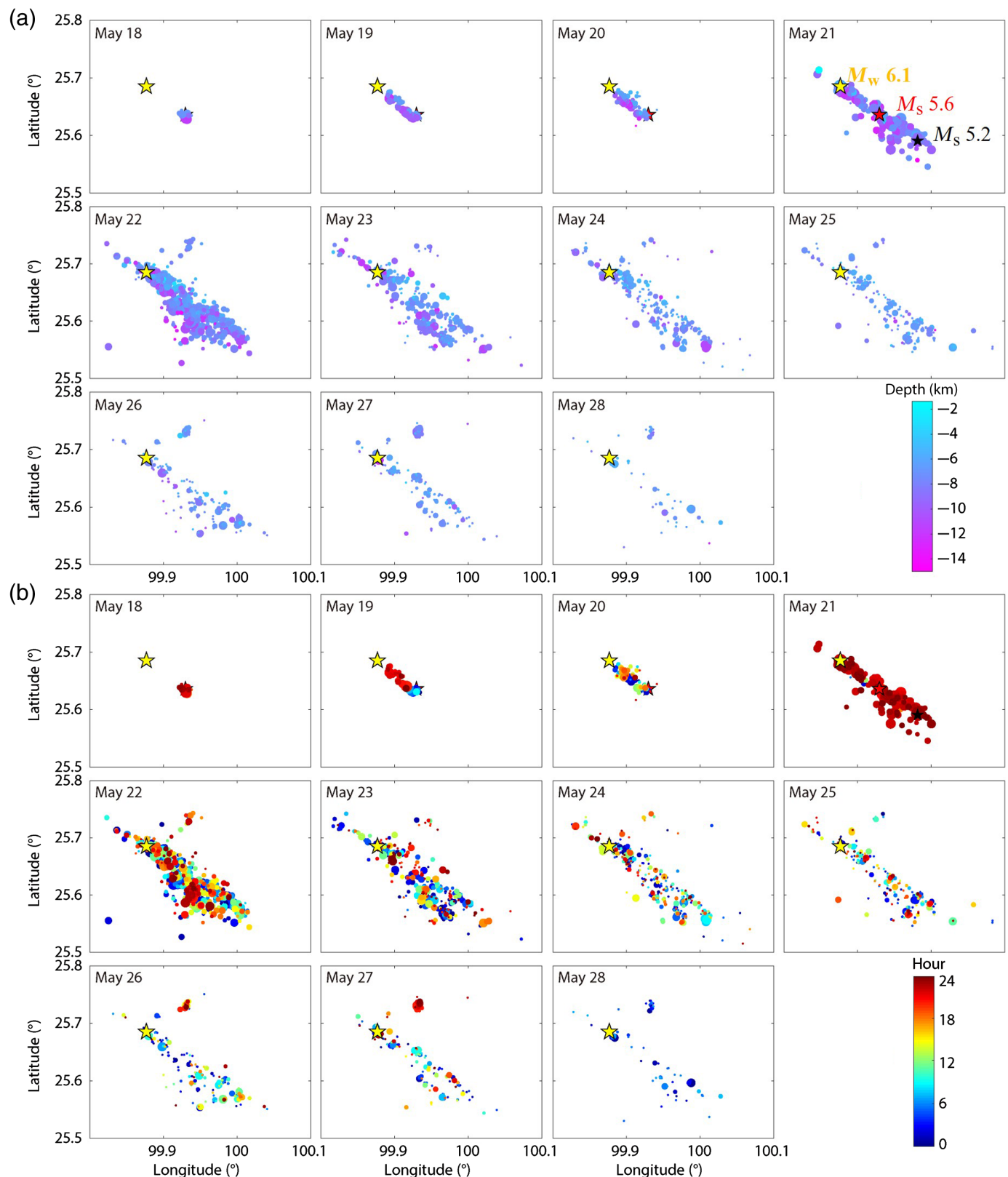


Figure 2. Seismicity distributions of the 2021 Yangbi earthquake. (a) Spatial-temporal seismicity distributions with color-coded depth, (b) spatial-temporal seismicity distributions with detailed color-coded time, and (c) seismicity plots of distance along fault

trace versus depth. The yellow, red, and black stars represent mainshock, largest foreshock, and aftershock, respectively. The color version of this figure is available only in the electronic edition.

(Continued)

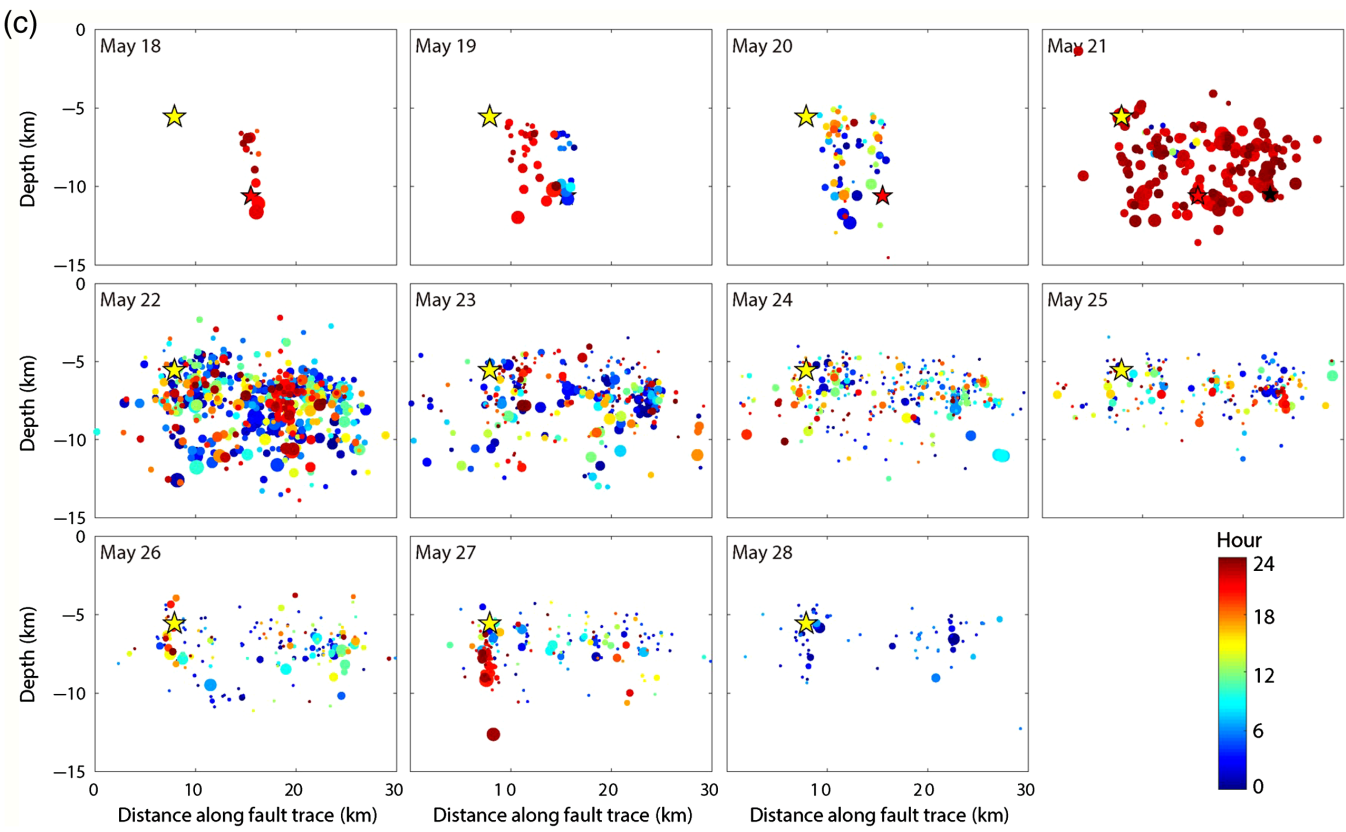


Figure 2. Continued

slip area is located at a depth of 2–10 km with a maximum slip of 0.8 m and has an average rake of $-163.8^{\circ}_{-0.33}^{+0.44}$ (Fig. 4a; Table S1). This indicates that the Yangbi earthquake is dominated by dextral strike slip with a minor normal slip component, reflecting the local tensional environment (Long *et al.*, 2021). This is in accordance with the existing seismological and geodetic studies (Wang *et al.*, 2021; Zhang, Gan, *et al.*, 2021). The seismogenic fault does not rupture to the surface, which is consistent with the field campaign observations (Li *et al.*, 2021). No clear surface rupture indicates a shallow slip deficit during the coseismic rupture, commonly observed in other strike-slip earthquakes (Brooks *et al.*, 2017). Projecting seismic relocations with magnitudes greater than M_s 4 onto the fault plane, we observed that these large aftershocks were located around the main slip area (Fig. 4b), demonstrating that the aftershocks are partially controlled by the stress change induced by the coseismic slip. The coseismic slip model effectively reproduced the surface geodetic displacements (Fig. 3b) with the root mean square of the residual of 0.6 cm for InSAR data (Fig. 3d), 0.68 cm for site YBZZ, 0.25 cm for site YBXL, 0.02 cm for site H204, and 0.89 cm for site YBZM. Assuming a shear modulus, $\mu = 34.5$ GPa (Laske *et al.*, 2013), the calculated seismic moment is 2.08×10^{18} N · m, which corresponds to a moment

magnitude of M_w 6.18. The slightly larger moment magnitude, compared to the existing reports (Table S1), may be attributed to the contributions of the aftershocks, postseismic relaxations, and possible different shear modulus.

Stress inversion results

The achieved temporal stress inversion results based on regional fault-plane solutions (Table S2), characterized by well-defined 95% confidence regions of principal stresses (Fig. 5), demonstrate stable stress fields in the 2021 Yangbi earthquake region with no clear temporal variations. The horizontal σ_1 axes with near north-south orientation coupled with horizontal σ_3 implies that the Yangbi earthquake region is under strike-slip stress regime (Tables S3). The near north-south maximum principal stress is comparable to the Global Positioning System (GPS) velocity vector in this region (Wang and Shen, 2020). However, it may be inferred that the largest fore-shock and mainshock have a certain disturbance to the localized stress fields illustrated by relatively larger α (Fig. 5), indicating that large earthquakes might cause temporary stress heterogeneity (Michael, 1991). This is in accordance with the variable strike slip, thrust, and normal earthquakes observed after the 2021 Yangbi earthquake (Long *et al.*, 2021).

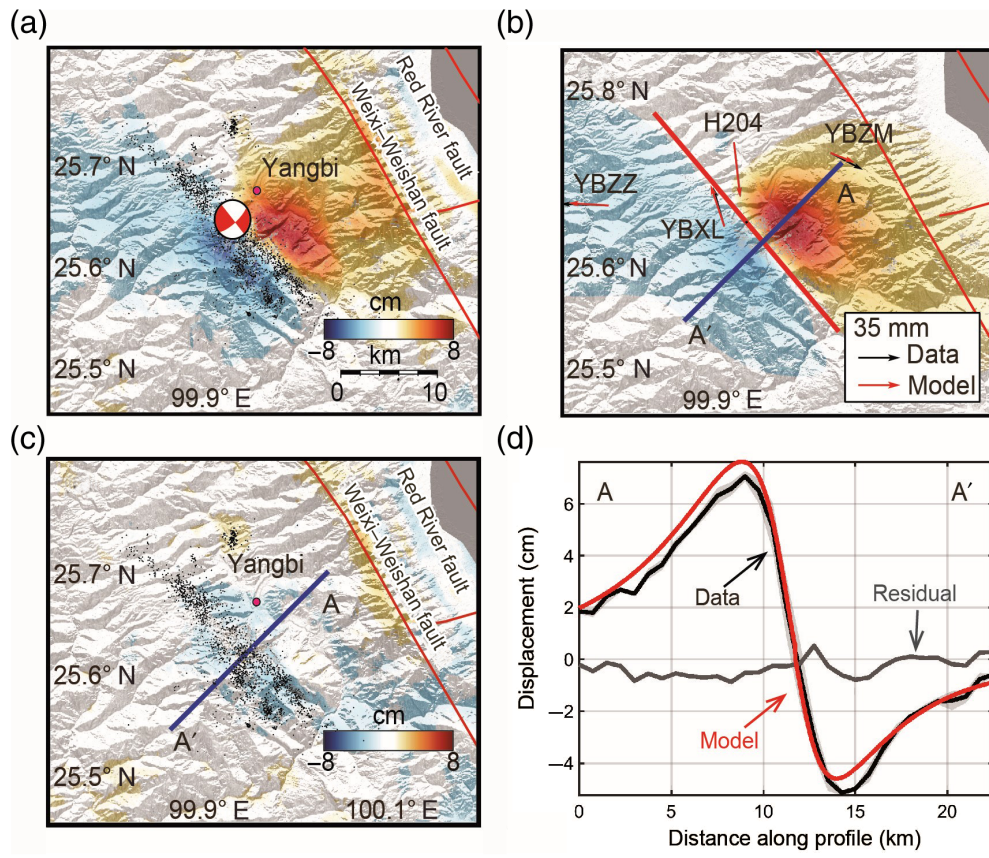


Figure 3. Coseismic deformation field and model prediction of the 2021 Yangbi earthquake. (a) The coseismic displacement map. The black dots represent the relocated earthquake sequences. The red focal mechanism plot is the focal mechanism solution from our geodetic inversion results. The red lines indicate the faults in the area. (b) The preferred model prediction. The Global Navigation Satellite Systems (GNSS) horizontal deformation is represented by black arrows with red arrows indicating the corresponding model predictions. The thick red line indicates the estimated fault trace. (c) The residual between data and model prediction. The blue line is a cross-fault profile shown in (d). (d) The Interferometric Synthetic Aperture Radar (InSAR) displacement and model prediction along the cross-fault profile in (b) and (c). The color version of this figure is available only in the electronic edition.

The derivation of the tectonic principal stress axes further permits us to decipher the type of fault. Following the scheme of stress regime characterization and maximum horizontal compressive stress orientation (SH_{\max}) proposed by Zoback (1992), based on the plunge and azimuth angles of the stress axes, we defined the temporal stress regimes in the Yangbi earthquake region as strike slip, with near east–west ($\sim 180^\circ$) temporal SH_{\max} (Table S3). These results are consistent with that from previous study (Long et al., 2021).

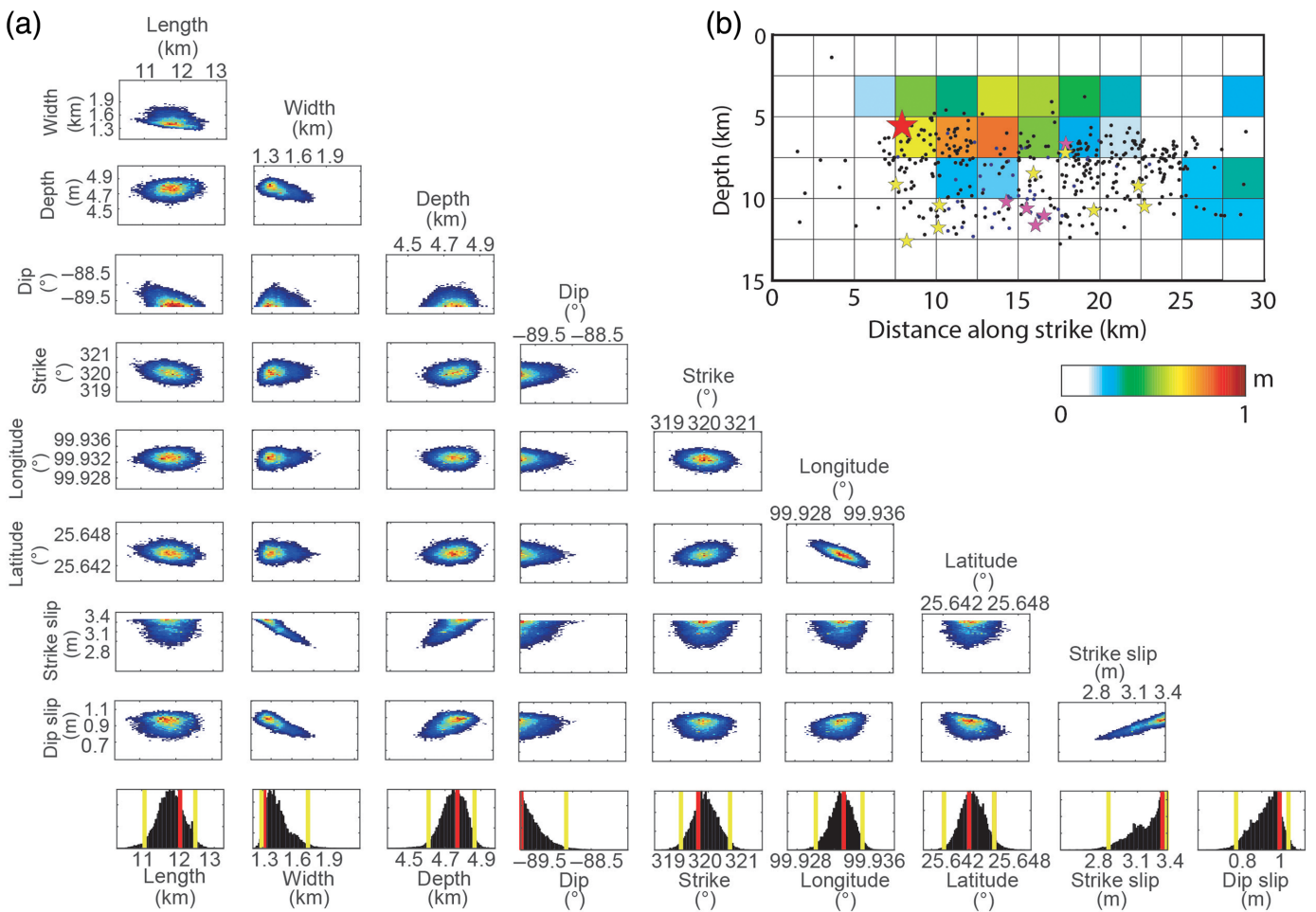
Discussions

Aseismic slip model and cascade triggering model

The 2021 Yangbi earthquake is a typical foreshock–mainshock–aftershock sequence with foreshocks occurring three days prior to the mainshock, which suggests an extended nucleation process (Soto et al., 2019; Kato and Ben-Zion, 2021). Recent studies

suggested that the cascade triggering model is more applicable to explain the Yangbi foreshock sequence because of the large radius (3 km) of its foreshock zone, incomprehensive fore-shock migrations, some quiescence windows, and reversal migration before the mainshock (Yang et al., 2021; Zhang et al., 2022). However, based on spectral ratio analysis and Coulomb stress change calculation, Zhou et al. (2021) proposed that Yangbi foreshock sequence is more than a simple triggered cascade, but combines multiple mechanisms (i.e., cascade, slow aseismic slip, and dynamic triggering). In our analysis, the detected foreshocks show migration fronts before the 2021 M_w 6.1 Yangbi earthquake (Figs. 2 and 6). The first front migrates to the hypocenter of large M_s 4.6 foreshock occurred on 19 May at an average speed of ~ 2 km/day during late 18 May and early 19 May (Fig. 6a,b), followed by a lull in foreshocks that lasted for ~ 12 hr. The second migration front propagates further to the northwest and migrates toward the mainshock at a higher speed of ~ 70 km/day (Fig. 6c). The seismicity zone also expands

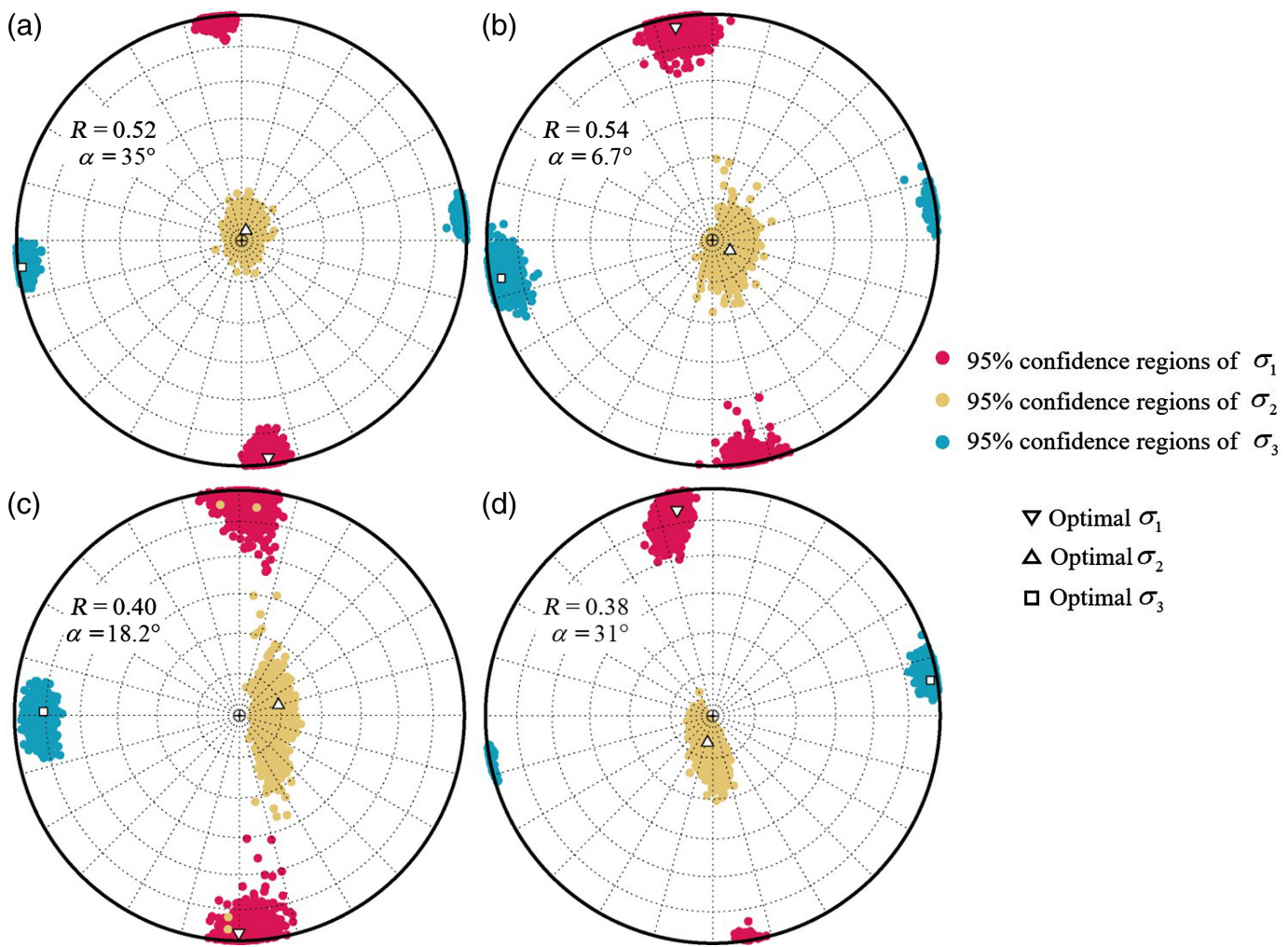
with time from southeast to northwest in the fault-trace direction (Fig. 2). These directional migrations indicate that the foreshocks between 18 and 19 May are probably byproducts of slow aseismic slip (i.e., afterslip of large events, slow-slip events, and other kinds of slow aseismic slip) during the nucleation process (Dodge et al., 1996; Kato et al., 2012; Jolivet and Frank, 2020). Almost all the events prior to the M_s 5.6 foreshock took place between the epicenters of the M_s 5.6 foreshock and the mainshock (Figs. 2 and 6a). This is comparable to that of the earthquake sequence before the 2011 M_w 9.0 Tohoku-Oki earthquake, which was triggered by the propagation of slow slip during the foreshock sequence (Kato et al., 2012). These spatio-temporal migrations along strike directions with logarithmic time may be attributed to the succession of several aseismic slip sequences of independent large foreshocks (i.e., afterslip of large foreshocks triggering other large foreshocks and/or mainshock;



(Matsuzawa *et al.*, 2004). Similarly, after the Yangbi mainshock, the aftershocks migrate to the southeast and northwest in along-strike direction with logarithmic time (Fig. 6a), supporting the view of aftershocks are driven primarily by afterslip (Peng and Zhao, 2009; Kato and Obara, 2014; Liu and Xu, 2019). This is consistent with the apparent postseismic deformation observed by GNSS after the 2021 Yangbi mainshock (Zhang, Gan, *et al.*, 2021) and the numerical simulations of aftershocks expansion caused by the propagating afterslip (Ariyoshi *et al.*, 2007; Kato, 2007; Perfettini *et al.*, 2018). In addition, obvious aftershock migration toward to southeast after the larges M_s 5.2 aftershock (Figs. 2 and 6a) could be driven by aseismic slip, comparable with the postseismic displacement progressing as a logarithmic function of time observed by GNSS (Zhang, Gan, *et al.*, 2021). This is similar with that observed after the 2007 M_w 6.7 Noto-Hanto earthquake (Kato and Obara, 2014), in which aftershocks are mainly attributed to afterslip boosted by an increase of shear stress around the mainshock rupture zone. Although the static stress triggering from the largest foreshock and the mainshock may also play a role in the occurrence of the largest aftershock. In addition, the cumulative number of aftershocks also increases with logarithmical time (Fig. 6), which is consistent well with numerical simulations based on the laboratory-derived rate-state-dependent friction law, indicating aftershocks expansion

Figure 4. Nonlinear and linear inversion of fault parameters. (a) The posterior probability distributions of fault geometry parameters. The red lines represent the maximum a posteriori probability solution with yellow lines indicating the 95% confidence region. The negative dip angles represent the inverted fault dipping southwest. (b) The coseismic slip distribution. The red star indicates the relocation of the mainshock. Foreshocks and aftershocks greater than M_s 4 are indicated by purple and yellow stars, respectively. The black dots indicate the relocations of aftershocks $M_s > 1$. The color version of this figure is available only in the electronic edition.

is driven by afterslip (Kato, 2007). These targeted foreshock and aftershock propagating fronts imply that slow aseismic slip have contributed to the nucleation processes of the large foreshocks, the mainshock, and the M_s 5.2 aftershock (Yao *et al.*, 2020), providing invaluable information for elucidating the preparatory processes of earthquake generation. This result is also consistent with recent foreshock sequences (Kato *et al.*, 2012; Ruiz *et al.*, 2014; Imanishi and Uchide, 2017; Soto *et al.*, 2019; Huang *et al.*, 2020), in which similar migration patterns of foreshock sequences have been associated with slow aseismic slip. Bouchon *et al.* (2013) suggested that ~70% of 31 interplate large earthquakes are preceded by a similar foreshock sequence



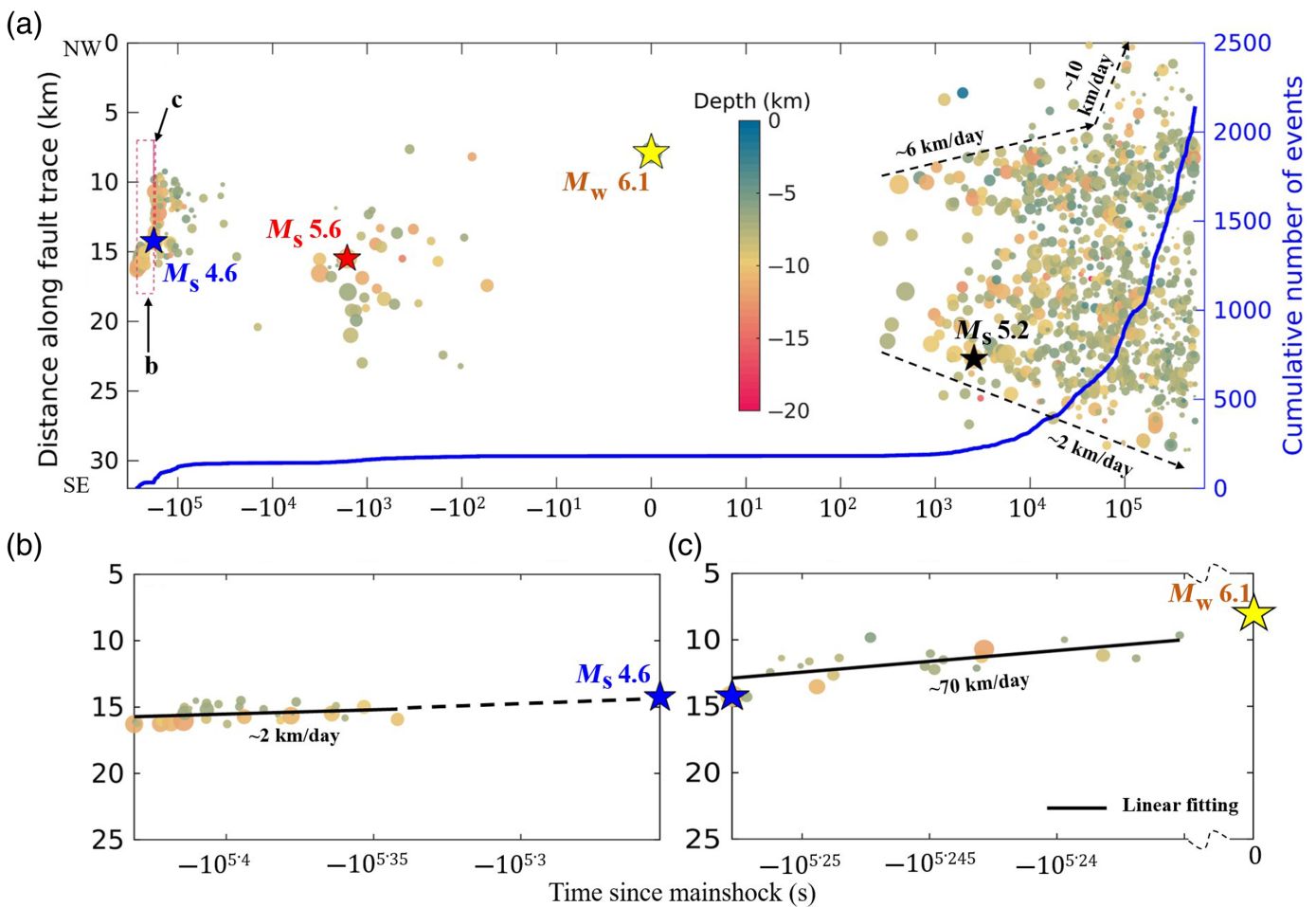
extension, which is attributed to slow slip before the interface rupture of the mainshocks. Moreover, laboratory experiments have suggested that more than 90% of the precursory moment during the nucleation process is released by aseismic slip (McLaskey and Lockner, 2014; Yamashita *et al.*, 2021).

In addition to the slow aseismic slip, the stress transfer imposed by the prior events on the latter also plays a significant role in promoting the failure of later events. We calculated the Coulomb stress change induced by two larger foreshocks on the largest M_s 5.6 foreshock (Fig. 7a; Table S4). In addition, an apparent negative Coulomb stress change is observed in the hypocenter of the largest foreshock, which is consistent with the source radius results characterized by significant source overlap near the hypocenter of the largest foreshock (Figs. 2 and 7c). This indicates the probable dominance of the aseismic slip in the nucleation process of the largest foreshock (Fig. 6). However, the source radius is scattered without overlap at the hypocenter of the mainshock, which prefers the cascade triggering model (Yao *et al.*, 2020). This is confirmed by the Coulomb stress change calculation when the largest foreshock is also introduced (Fig. 7b; Table S4). This exhibits that approximately 0.03 MPa stress triggers are observed at the nucleation point of the mainshock. The positive Coulomb

Figure 5. Stress inversion results from focal mechanisms in Yangbi earthquake region for different time intervals. (a) 1970 to 18 May 2021, (b) 18 May 2021–largest foreshock, (c) largest foreshock–mainshock, and (d) aftershocks. The color version of this figure is available only in the electronic edition.

stress change is larger than the typical triggering threshold of ~ 0.01 MPa (Hardebeck *et al.*, 1998), indicating that the triggering mechanism of stress transfer (cascade model) is also crucial in the nucleation process of the 2021 Yangbi mainshock (Kato *et al.*, 2016).

In summary, it is likely that slow aseismic slip plays a dominant role in the nucleation process of the largest foreshock (Fig. 7a,c), and the stress transfer from both aseismic and seismic slip during the foreshock sequence promotes the failure of the mainshock (Figs. 6 and 7b). This may imply that slow aseismic slip during the Yangbi foreshock weakens the fault producing the largest foreshock, which eventually cascade to initiate the dynamic rupture of the 2021 Yangbi mainshock. Similar phenomena have been observed in the 2016 M_w 7.1 Kumamoto earthquake (Kato *et al.*, 2016) and the 2010 M_w 7.2 El Mayor–Cucapah earthquake (Yao *et al.*, 2020) as



well as in the laboratory experiments (McLaskey and Lockner, 2014; Yamashita *et al.*, 2021). Except for the static stress triggering of large foreshocks and the mainshock, the aftershocks could be mainly explained by afterslip. In addition to the multiple stress transfer (i.e., slow aseismic slip and cascade triggering), we cannot rule out the relative importance of fluid diffusion during the Yangbi earthquake sequence (Miller, 2020).

Possible driving mechanisms of the 2021 Yangbi earthquake

The 2021 Yangbi earthquake occurred in an area of high moment deficit with a ratio of ~ 5 between the seismic moment accumulation and release (Zhao *et al.*, 2020). Moreover, it is located in an area with a low b -value of 0.5 (Xie *et al.*, 2015), which implies that the Yangbi earthquake is in a state of high-stress concentration before its occurrence. This is in accordance with the high shear rate of $\sim 2 \times 10^{-8}/\text{yr}$ estimated by GPS observations (Wang and Shen, 2020). Our temporal stress inversion results based on the focal mechanism solutions (Table S2) demonstrate that the maximum principal stress direction is near north-south without evident temporal variations in the Yangbi earthquake region (Fig. 5). This is consistent with the directions of the majority of the strike-slip faults in the region, the current GPS movement direction (Wang and

Figure 6. (a) Plots of distance along fault trace versus logarithmic time exhibiting the temporal evolution of the foreshock and aftershocks. Earthquakes are colored by depth and scaled by magnitude. The M_s 4.6 foreshock, the largest M_s 5.6 foreshock, the mainshock, and the largest M_s 5.2 aftershock are plotted as blue, red, yellow, and black stars, respectively. Blue line indicates the cumulative number of events. The black dashed lines with arrows mark the approximate aftershock migration along the causative fault. (b,c) The zoom-in of dashed boxes in (a) with different time windows. The dashed line in (b) is the extension of linear fitting. The black lines show the linear fittings, indicating approximate migration fronts labeled by migration rates. The labeled migration speeds are the mean velocity within specific time window. The color version of this figure is available only in the electronic edition.

Shen, 2020; Zhang, Liang, *et al.*, 2021) and the crustal anisotropy direction in the upper crust (Gao *et al.*, 2020). As the focal mechanism solutions utilized in the stress inversion are mostly located in the upper crust, our stress inversion results reflect the stress state in the upper crust. Thus, the lateral material extrusion in the upper crust is a possible driving mechanism of the Yangbi earthquake (Fig. 8). This is consistent with the InSAR- and GNSS-based fault slip dominated by right-lateral strike slip (Fig. 4).

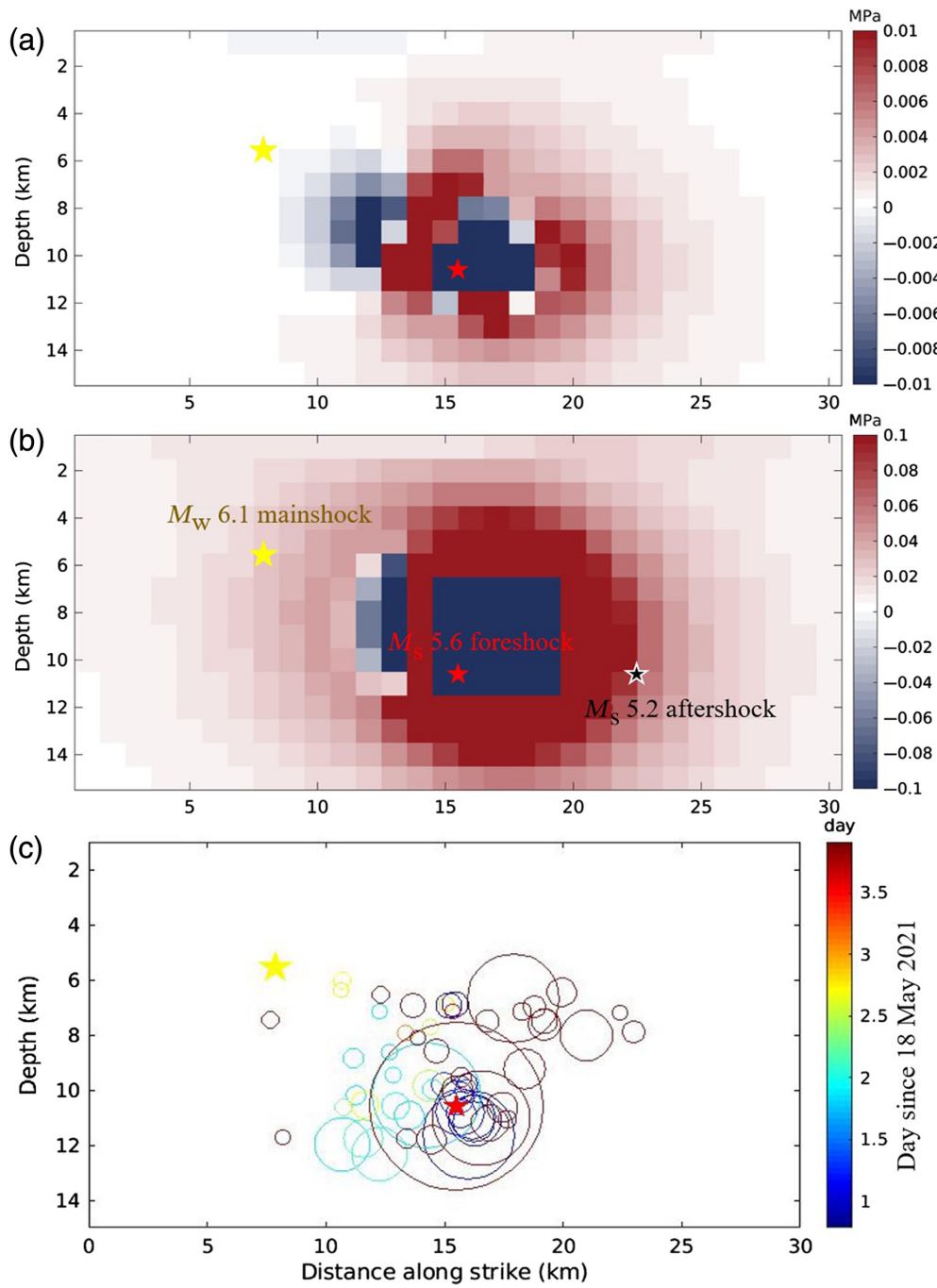


Figure 7. (a) Coulomb stress change induced by M_s 4.5 and 4.3 foreshocks. The red and yellow stars represent largest foreshock and mainshock, respectively. (b) Coulomb stress change induced by M_s 4.5, 4.3, and 5.6 (red star) foreshocks. (c) Displays the foreshock sequence events colored by time and sized by the source radius, which is estimated based on the a circular crack model $R = \left(\frac{16\Delta\sigma}{7M_0}\right)^{1/3}$ assuming a stress drop of 3 MPa (Eshelby, 1957). The color version of this figure is available only in the electronic edition.

In addition, the velocity structure imaged by the joint inversion of surface-wave dispersion and receiver functions exhibits a conspicuous low-velocity layer (~ 20 km at depth) beneath the Yangbi earthquake (Bao *et al.*, 2015; Huang *et al.*,

2021), which is consistent with the velocity structure revealed by the joint inversion of body- and surface-wave travel-time tomography (Liu *et al.*, 2021) and high heat flow beneath the study area (Hu *et al.*, 2000). Bai *et al.* (2010) suggested two channels of high conductivity based on magnetotelluric images, which have been interpreted as distinct crustal flow channels. Using teleseismic Rayleigh wave and ambient noise data, Zhang *et al.* (2020) further observed a well-connected channel of low-velocity zone corresponding to channel A in Bai *et al.* (2010) and another isolate low-velocity zone. This is in agreement with the corresponding high Lg -wave attenuation tomography. The Yangbi earthquake occurred near the west crust flow channel (channel A) along the Nujiang fault. Thus, the crust channel flow probably plays a significant role in facilitating shear strain and earthquake nucleation (Gao *et al.*, 2021). Jointly, these results suggest that crust channel flow is probably the deeper driving force of the 2021 Yangbi earthquake (Fig. 8). In addition, because the Yangbi earthquake occurred on the southwestern edge of the Sichuan-Yunnan block, the blockage of the inner belt of the rigid Emeishan large igneous province may also play an important role both in the accumulation and release of shear stress, as confirmed by the high-velocity anomaly

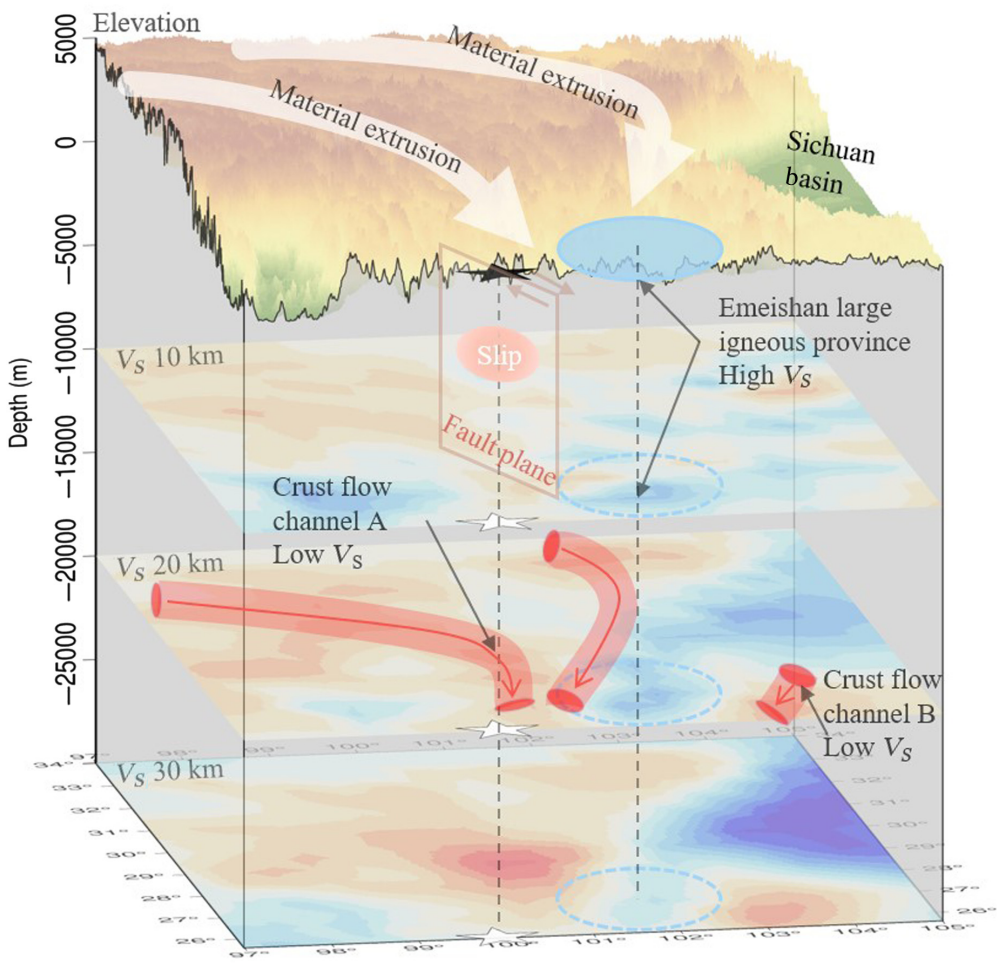


Figure 8. Schematic cartoon illustrates the possible driving forces including the upper lateral material extrusion and lower crust flow channel. Color maps represent S-wave velocity models at selected depths of 10, 20, and 30 km from southwest China community velocity model 1.0 (CVM-1.0; Liu *et al.*, 2021), respectively. The black star represents the 2021 Yangbi mainshock. The fault plane, crust flow channels, and Emeishan large igneous province are not scaled. The color version of this figure is available only in the electronic edition.

Relationships between aftershock distributions and Coulomb stress change

Seismic stress triggering theory indicates that accumulated tectonic stress released suddenly during earthquakes will be redistributed and probably perturb the surrounding faults (King *et al.*, 1994). To probe the relationship between aftershocks and stress perturbation induced by coseismic slip, we calculated the static Coulomb failure stress changes (ΔCFS) triggered by the Yangbi mainshock on the seismogenic fault (Lin and Stein, 2004) with an effective frictional coefficient of $\mu = 0.4$.

A peak positive static ΔCFS of up to 3.1 MPa is observed around the coseismic slip zone (Fig. 9). Eight out of the nine aftershocks ($M_s > 4$) are observed in the positive static ΔCFS area. This indicates that these large aftershocks are partially triggered by the static Coulomb stress change after the mainshock (Freed, 2005). In addition, the prevailing postseismic

relaxation after a large earthquake (e.g., afterslip) triggered by the redistribution of stress and significantly influences the aftershock distribution (Freed, 2005), which is confirmed by the apparent post-seismic displacement observed by GNSS after the Yangbi mainshock (fig. 3 in Zhang, Gan, *et al.*, 2021). Notably, the aftershock distribution has a strong relationship with the stress shadow at a relatively shallow depth, whereas the relatively deeper part exhibits a strong correlation between aftershocks and stress triggers (Fig. 9). This implies that the stress state along the dip direction may be heterogeneous owing to multiple failures of small asperities (Rydelek and Sacks, 1999). The occurrence of aftershocks in the region of stress shadows could also be attributed to the oversimplification of seismogenic fault, small faults with different azimuth orientations, and/or heterogeneities of crustal properties (Freed, 2005). Moreover, aftershock-related stress shadows can also be observed with significant seismicity before an earthquake (Freed, 2005), sim-

ilar to those foreshocks observed prior to the 2021 Yangbi earthquake.

In addition, very few aftershocks occurred at shallow depths, which displays apparent strong statics ΔCFS . This can be attributed to the presence of poorly consolidated shallow sediments, which are often characterized by velocity-strengthening frictional properties favoring aseismic slip. This generally impedes the rupture propagation during the mainshock (Brooks *et al.*, 2017), which is confirmed by the observed shallow slip deficit during the Yangbi earthquake (Fig. 4b). The strong static stress triggers in the shallow crust may further trigger shallow postseismic aseismic slip or inelastic deformation, which is consistent with the apparent postseismic displacement after the mainshock (fig. 3 in Zhang, Gan, *et al.*, 2021). This will partially compensate for the shallow slip deficit observed in the Yangbi earthquake.

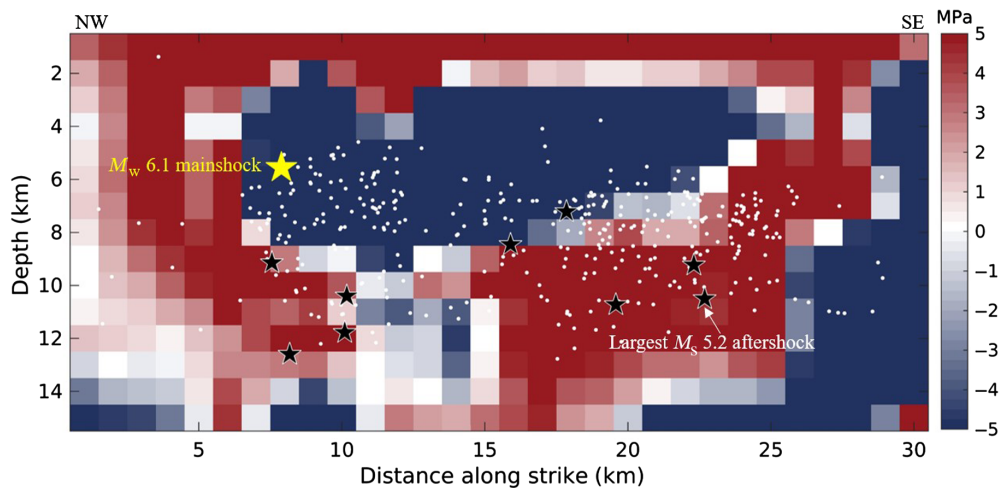


Figure 9. Relationships between aftershocks distribution and static Coulomb stress change on seismogenic fault interface, as induced by the 2021 Yangbi earthquake. The white dots and black stars indicate the relocated aftershocks ($M_s > 1$) and larger aftershocks ($M_s > 4$), respectively. The color version of this figure is available only in the electronic edition.

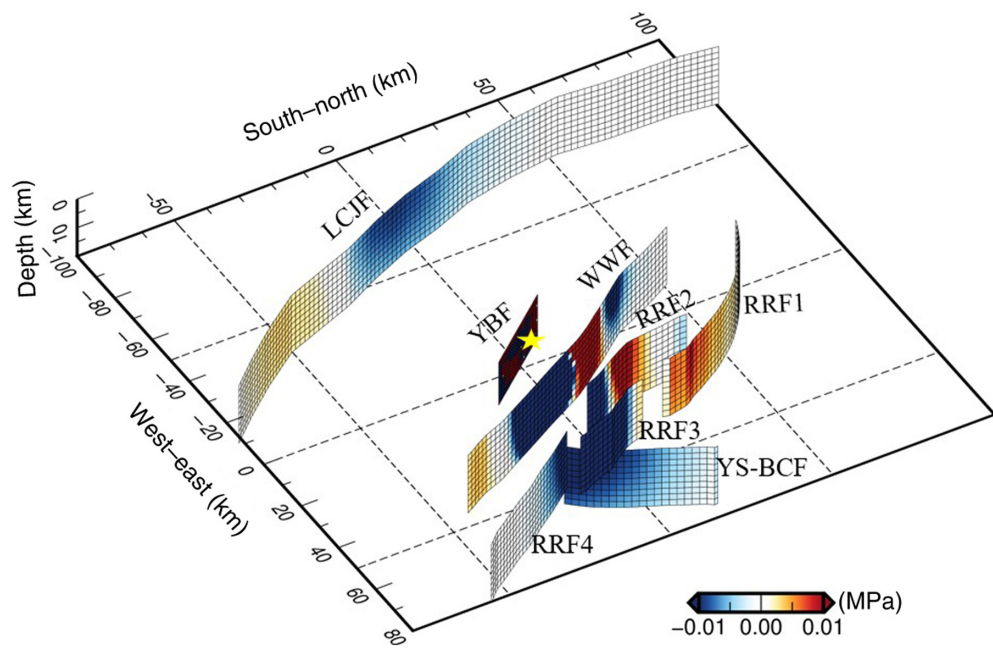


Figure 10. Distribution of the static Δ CFS in the adjacent active faults caused by the 2021 Yangbi earthquake. The yellow star represents the relocated hypocenter. The geometries of the receiver faults are determined based on the information of active faults in China. Color scale is saturated at $[-0.01, 0.01]$ MPa for the visualization. LCJF, Lancangjiang fault; RRF1-4, Red River fault 1-4; WWF, Weixi-Weishan fault; YBF, Yangbi fault; YS-BCF, Yongsheng-Binchuan fault. The color version of this figure is available only in the electronic edition.

Regional seismic hazard

The 2021 Yangbi M_w 6.1 earthquake is the strongest earthquake recorded instrumentally during the last half-century within 100 km of the epicenter. Hence, it is crucial to evaluate the

influence of the 2021 Yangbi earthquake on its adjacent active faults. Implementing the same Coulomb stress change calculation method in the **Relationships between aftershock distributions and Coulomb stress change** section and adopting the coseismic slip model caused by the mainshock as the source, we calculated the static Coulomb failure stress changes (Δ CFS) on the adjacent active faults to evaluate the regional seismic hazards (Lin and Stein, 2004). A Δ CFS increase of 0.09 MPa is observed in the central part of the Weixi-Weishan fault (WWF), which is a normal dextral-slip fault located in the eastern side of the Yangbi earthquake epicenter (Fig. 10). We also observe a peak Δ CFS increase of 0.01 and 0.03 MPa on Red River faults (RRFs), that is, RRF1 and RRF2, respectively. In addition, a relatively small positive zone is observed at the southern tip of the Lancangjiang fault (Fig. 10). The calculated positive Δ CFS on the adjacent faults (central WWF, RRF1-2) exceeds the earthquake triggering threshold of 0.01 MPa (Hardebeck *et al.*, 1998). This indicates that the seismic hazard for these faults may potentially increase, especially for WWF and RRF2. Considering that the city of Dali encircled by the WWF and RRF2 contains a population of over 600,000, we suggest that the potential seismic hazard should be taken into consideration in the future.

Conclusions

The 2021 M_w 6.1 Yangbi earthquake caused by a rupture of a blind fault located at the southeastern margin of the Tibetan plateau; the earthquake represents a typical foreshock–mainshock–

aftershock event. The InSAR and GNSS observations can be well explicated by the fault slip on a vertical fault plane with a strike angle of 320°. Coseismic slip is dominated by right-lateral strike slip with a peak value of 0.8 m. Combining the stress triggers from foreshocks on the mainshock, the apparent migrations of relocated foreshocks to the large M_s 4.6 foreshock and the mainshock hypocenters support the combined effects of aseismic slip and cascading failure that led to the mainshock. The stress inversion results with no evident temporal variations indicate a constant driving force beneath the Yangbi earthquake region. The maximum principal stress direction near north–south is consistent with the GPS velocity vectors and crustal anisotropy direction. By combining low velocity, high conductivity, and high Lg -wave attenuation beneath the Yangbi region, we infer that the lateral upper crustal extrusion and lower crust flow are possible driving mechanisms for the Yangbi earthquake. The relationship between aftershock distribution and static Coulomb stress change indicates that eight of the nine large aftershocks ($M_s > 4$) can be explained by coseismic stress perturbations and postseismic relaxations. For future endeavors, denser seismic stations are required to precisely relocate an earthquake sequence with a small magnitude of completeness. Furthermore, we believe that the ongoing efforts will improve our understanding of the nucleation processes of large earthquakes.

Data and Resources

Raw Sentinel-1A data are available at <https://scihub.copernicus.eu/dhus/#/home> (last accessed July 2021). The GAMMA commercial software is obtained from <https://www.gamma-rs.ch/software> (last accessed July 2021). The GBIS software is obtained from <https://comet.nerc.ac.uk/gbis/> (last accessed August 2021). ERA5 data is available from <http://climate.copernicus.eu/products/climate-reanalysis> (last accessed August 2021). The iterative joint stress inversion software is obtained from <https://www.ig.cas.cz/en/stress-inverse/> (last accessed August 2021). The Coulomb3 software is available at <https://www.usgs.gov/node/279387> (last accessed August 2021). The Generic Mapping Tools (GMT) created figures are obtained from <https://www.generic-mapping-tools.org/> (last accessed August 2021). Regional faults are obtained from <http://datashare.igl.earthquake.cn/map/ActiveFault/introFault.html> (last accessed August 2021). Some focal mechanisms are available from the EarthX reporting system (<http://124.17.4.85/?p=544>, last accessed August 2021). The supplemental material includes Tables S1–S4.

Declaration of Competing Interests

The authors acknowledge that there are no conflicts of interest recorded.

Acknowledgments

The authors are deeply indebted to Editor Allison Bent and Associate Editor, Yen Joe Tan and another anonymous reviewer for their constructive reviews and comments. The authors would also like to extend their sincere thanks to Aitaro Kato, William L. Ellsworth, Futoshi Yamashita, Zhigang Peng, Huajian Yao, Weijun Gan, Hui

Huang, and Dongdong Yao for their valuable suggestions, data sharing, and communications during the development of this work. This work was supported by National Key R&D Program of China (Grant Number 2019YFC1509205), National Natural Science Foundation of China (Grant Number 42174023), and the Innovation Foundation for Postgraduate of Central South University (Grant Number 2020zzts181) and by the Hunan Provincial Innovation Foundation for Postgraduate (Grant Number CX20200344).

References

- Amey, R., A. Hooper, and R. Walters (2018). A Bayesian method for incorporating self-similarity into earthquake slip inversions, *J. Geophys. Res.* **123**, 6052–6071.
- Ariyoshi, K., T. Matsuzawa, and A. Hasegawa (2007). The key frictional parameters controlling spatial variations in the speed of postseismic-slip propagation on a subduction plate boundary, *Earth Planet. Sci. Lett.* **256**, 136–146.
- Bagnardi, M., and A. Hooper (2018). Inversion of surface deformation data for rapid estimates of source parameters and uncertainties: A Bayesian approach, *Geochem. Geophys. Geosys.* **19**, 2194–2211.
- Bai, D., M. J. Unsworth, M. A. Meju, X. Ma, J. Teng, X. Kong, Y. Sun, J. Sun, L. Wang, C. Jiang, et al. (2010). Crustal deformation of the eastern Tibetan plateau revealed by magnetotelluric imaging, *Nature Geosci.* **3**, 358–362.
- Bao, X., X. Sun, M. Xu, D. W. Eaton, X. Song, L. Wang, Z. Ding, N. Mi, H. Li, and D. Yu (2015). Two crustal low-velocity channels beneath SE Tibet revealed by joint inversion of Rayleigh wave dispersion and receiver functions, *Earth Planet. Sci. Lett.* **415**, 16–24.
- Beroza, G. C., and W. L. Ellsworth (1996). Properties of the seismic nucleation phase, *Tectonophysics* **261**, 209–227.
- Bouchon, M., V. Durand, D. Marsan, H. Karabulut, and J. Schmittbuhl (2013). The long precursory phase of most large interplate earthquakes, *Nature Geosci.* **6**, 299–302.
- Bouchon, M., H. Karabulut, M. Aktar, S. Ozalaybey, J. Schmittbuhl, and M. P. Bouin (2011). Extended nucleation of the 1999 Mw 7.6 Izmit earthquake, *Science* **331**, 877–880.
- Brooks, B. A., S. E. Minson, C. L. Glennie, J. M. Nevitt, T. Dawson, R. Rubin, T. L. Ericksen, D. Lockner, K. Hudnut, and V. Langenheim (2017). Buried shallow fault slip from the South Napa earthquake revealed by near-field geodesy, *Sci. Adv.* **3**, e1700525, doi: [10.1126/sciadv.1700525](https://doi.org/10.1126/sciadv.1700525).
- Cao, Y., S. Jónsson, and Z. Li (2021). Advanced InSAR tropospheric corrections from global atmospheric models that incorporate spatial stochastic properties of the troposphere, *J. Geophys. Res.* **126**, e2020JB020952, doi: [10.1029/2020JB020952](https://doi.org/10.1029/2020JB020952).
- Chen, C. W., and H. A. Zebker (2002). Phase unwrapping for large SAR interferograms: Statistical segmentation and generalized network models, *IEEE Trans. Geosci. Remote Sens.* **40**, 1709–1719.
- Chen, X., and P. M. Shearer (2013). California foreshock sequences suggest aseismic triggering process, *Geophys. Res. Lett.* **40**, 2602–2607.
- Dodge, D. A., G. C. Beroza, and W. Ellsworth (1996). Detailed observations of California foreshock sequences: Implications for the earthquake initiation process, *J. Geophys. Res.* **101**, 22,371–22,392.
- Ellsworth, W. L., and F. Bulut (2018). Nucleation of the 1999 Izmit earthquake by a triggered cascade of foreshocks, *Nature Geosci.* **11**, 531–535.

- Eshelby, J. D. (1957). The determination of the elastic field of an ellipsoidal inclusion, and related problems, *Proc. Roy. Soc. Lond.* **241**, 376–396, doi: [10.1098/rspa.1957.0133](https://doi.org/10.1098/rspa.1957.0133).
- Farr, T. G., P. A. Rosen, E. Caro, R. Crippen, R. Duren, S. Hensley, M. Kobrick, M. Paller, E. Rodriguez, L. Roth, *et al.* (2007). The shuttle radar topography mission, *Rev. Geophys.* **45**, no. 2, doi: [10.1029/2005RG000183](https://doi.org/10.1029/2005RG000183).
- Freed, A. M. (2005). Earthquake triggering by static, dynamic, and post-seismic stress transfer, *Annu. Rev. Earth Planet. Sci.* **33**, 335–367.
- Gao, T., Z. Ding, X. Wang, and L. Jiang (2021). Joint inversion of receiver functions, Rayleigh wave dispersion and ZH ratio for crustal structure in southeast Tibetan plateau and its implications for dynamics, *Chin. J. Geophys.* **64**, 1885–1906.
- Gao, Y., Y. Shi, and Q. Wang (2020). Seismic anisotropy in the southeastern margin of the Tibetan plateau and its deep tectonic significances, *Chin. J. Geophys.* **63**, 802–816.
- Hardebeck, J. L., J. J. Nazareth, and E. Hauksson (1998). The static stress change triggering model: Constraints from two southern California aftershock sequences, *J. Geophys. Res.* **103**, 24,427–24,437.
- Hu, X. (2020). *The Study of Tectonic Stress Field in Yunnan and its Adjacent Areas*, Institute of Disaster Prevention, China, doi: [10.27899/d.cnki.gfzkj.2020.000029](https://doi.org/10.27899/d.cnki.gfzkj.2020.000029) (in Chinese).
- Hu, S., L. He, and J. Wang (2000). Heat flow in the continental area of China: A new data set, *Earth Planet. Sci. Lett.* **179**, 407–419.
- Huang, H., L. Meng, R. Bürgmann, W. Wang, and K. Wang (2020). Spatio-temporal foreshock evolution of the 2019 M 6.4 and M 7.1 Ridgecrest, California earthquakes, *Earth Planet. Sci. Lett.* **551**, doi: [10.1016/j.epsl.2020.116582](https://doi.org/10.1016/j.epsl.2020.116582).
- Huang, Z., C. Ji, H. Wu, Y. Shi, J. Geng, M. Xu, C. Han, and L. Wang (2021). Reviews on the crustal structures and deformations in the southeastern margin of the Tibetan plateau, *Rev. Geophys. Planet. Phys.* **52**, no. 3, 291–307.
- Imanishi, K., and T. Uchide (2017). Non-self-similar source property for microforeshocks of the 2014 Mw 6.2 northern Nagano, central Japan, earthquake, *Geophys. Res. Lett.* **44**, 5401–5410.
- Jolivet, R., and W. Frank (2020). The transient and intermittent nature of slow slip, *AGU Adv.* **1**, e2019AV000126, doi: [10.1029/2019AV000126](https://doi.org/10.1029/2019AV000126).
- Kato, N. (2007). Expansion of aftershock areas caused by propagating post-seismic sliding, *Geophys. J. Int.* **168**, 797–808.
- Kato, A., and Y. Ben-Zion (2021). The generation of large earthquakes, *Nat. Rev. Earth Environ.* **2**, 26–39.
- Kato, A., and K. Obara (2014). Step-like migration of early aftershocks following the 2007 Mw 6.7 Noto-Hanto earthquake, Japan, *Geophys. Res. Lett.* **41**, 3864–3869.
- Kato, A., J. I. Fukuda, S. Nakagawa, and K. Obara (2016). Foreshock migration preceding the 2016 Mw 7.0 Kumamoto earthquake, Japan, *Geophys. Res. Lett.* **43**, 8945–8953.
- Kato, A., K. Obara, T. Igarashi, H. Tsuruoka, S. Nakagawa, and N. Hirata (2012). Propagation of slow slip leading up to the 2011 Mw 9.0 Tohoku-Oki earthquake, *Science* **335**, 705–708.
- King, G. C., R. S. Stein, and J. Lin (1994). Static stress changes and the triggering of earthquakes, *Bull. Seismol. Soc. Am.* **84**, 935–953.
- Laske, G., G. Masters, Z. Ma, and M. Pasyanos (2013). Update on CRUST1. 0—A 1-degree global model of Earth's crust, *EGU General Assembly 2013*, Vienna, Austria, 7–12 April 2013, ID EGU2013-2658.
- Lei, X., Z. Wang, S. Ma, and C. He (2021). A preliminary study on the characteristics and mechanism of the May 2021 Ms 6.4 Yangbi earthquake sequence, Yunnan, China, *Acta Seismol. Sinica* **43**, 261–286 (in Chinese).
- Li, C., J. Zhang, W. Wang, K. Sun, and X. Shan (2021). The seismogenic fault of the 2021 Yunnan Yangbi Ms6.4 earthquake, *Seismol. Geol.* **43**, no. 3, 706–721.
- Li, X., X. Ma, Y. Chen, S. Xue, I. M. Varentsov, and D. Bai (2020). A plume-modified lithospheric barrier to the southeastward flow of partially molten Tibetan crust inferred from magnetotelluric data, *Earth Planet. Sci. Lett.* **548**, doi: [10.1016/j.epsl.2020.116493](https://doi.org/10.1016/j.epsl.2020.116493).
- Li, Z., X. Ding, C. Huang, J. Zhu, and Y. Chen (2008). Improved filtering parameter determination for the Goldstein radar interferogram filter, *ISPRS J. Photogramm. Remote Sens.* **63**, 621–634.
- Lin, J., and R. S. Stein (2004). Stress triggering in thrust and subduction earthquakes and stress interaction between the southern San Andreas and nearby thrust and strike-slip faults, *J. Geophys. Res.* **109**, no. B2, doi: [10.1029/2003JB002607](https://doi.org/10.1029/2003JB002607).
- Liu, X., and W. Xu (2019). Logarithmic model joint inversion method for coseismic and postseismic slip: Application to the 2017 Mw 7.3 Sarpol Zahab earthquake, Iran[J], *J. Geophys. Res.* **124**, no. 11, 12,034–12,052, doi: [10.1029/2019JB017953](https://doi.org/10.1029/2019JB017953).
- Liu, Y., H. Yao, H. Zhang, and H. Fang (2021). The community velocity model V.1.0 of southwest China, constructed from joint body- and surface-wave travel-time tomography, *Seismol. Res. Lett.* **92**, no. 5, 2972–2987.
- Long, F., Y. Qi, G. Yi, W. Wu, G. Wang, X. Zhao, and G. Peng (2021). Relocation of the M_s 6.4 Yangbi earthquake sequence on May 21, 2021 in Yunnan province and its seismogenic structure analysis, *Chin. J. Geophys.* **64**, 2631–2646.
- Lund, B., and R. Slunga (1999). Stress tensor inversion using detailed microearthquake information and stability constraints: Application to Ölfus in southwest Iceland, *J. Geophys. Res.* **104**, 14,947–14,964.
- Marsan, D., and B. Enescu (2012). Modeling the foreshock sequence prior to the 2011, M_W 9.0 Tohoku, Japan, earthquake, *J. Geophys. Res.* **117**, no. B6, doi: [10.1029/2011JB009039](https://doi.org/10.1029/2011JB009039).
- Matsuzawa, T., N. Uchida, T. Igarashi, T. Okada, and A. Hasegawa (2004). Repeating earthquakes and quasi-static slip on the plate boundary east off northern Honshu, Japan, *Earth Planets Space* **56**, 803–811.
- McLaskey, G. C., and D. A. Lockner (2014). Preslip and cascade processes initiating laboratory stick slip, *J. Geophys. Res.* **119**, 6323–6336.
- Michael, A. J. (1987). Use of focal mechanisms to determine stress: A control study, *J. Geophys. Res.* **92**, 357–368.
- Michael, A. J. (1991). Spatial variations in stress within the 1987 Whittier Narrows, California, aftershock sequence: New techniques and results, *J. Geophys. Res.* **96**, 6303–6319.
- Miller, S. A. (2020). Aftershocks are fluid-driven and decay rates controlled by permeability dynamics, *Nat. Commun.* **11**, doi: [10.1038/s41467-020-19590-3](https://doi.org/10.1038/s41467-020-19590-3).
- Okada, Y. (1985). Surface deformation due to shear and tensile faults in a half-space, *Bull. Seismol. Soc. Am.* **75**, 1135–1154.
- Peng, Z. G., and P. Zhao (2009). Migration of early aftershocks following the 2004 Parkfield earthquake, *Nature Geosci.* **2**, 877–881.

- Perfettini, H., W. B. Frank, D. Marsan, and M. Bouchon (2018). A model of aftershock migration driven by afterslip, *Geophys. Res. Lett.* **45**, 2283–2293.
- Prats-Iraola, P., R. Scheiber, L. Marotti, S. Wollstadt, and A. Reigber (2012). TOPS interferometry with TerraSAR-X, *IEEE Trans. Geosci. Remote Sens.* **50**, 3179–3188.
- Ross, Z. E., E. S. Cochran, D. T. Trugman, and J. D. Smith (2020). 3D fault architecture controls the dynamism of earthquake swarms, *Science* **368**, 1357–1361.
- Ruiz, S., M. Metois, A. Fuenzalida, J. Ruiz, F. Leyton, R. Grandin, C. Vigny, R. Madariaga, and J. Campos (2014). Intense foreshocks and a slow slip event preceded the 2014 Iquique Mw 8.1 earthquake, *Science* **345**, 1165–1169.
- Rydelek, P. A., and I. S. Sacks (1999). Large earthquake occurrence affected by small stress changes, *Bull. Seismol. Soc. Am.* **89**, 822–828.
- Soto, H., C. Sippl, B. Schurr, J. Kummerow, G. Asch, F. Tilmann, D. Comte, S. Ruiz, and O. Oncken (2019). Probing the northern Chile megathrust with seismicity: The 2014 M8.1 Iquique earthquake sequence, *J. Geophys. Res.* **124**, 12,935–12,954.
- Su, J., M. Liu, Y. Zhang, W. Wang, H. Li, J. Yang, X. Li, and M. Zhang (2021). High resolution earthquake catalog building for the 21 May 2021 Yangbi, Yunnan, M_s 6.4 earthquake sequence using deep-learning phase picker, *Chin. J. Geophys.* **64**, 2647–2656.
- Vavryčuk, V. (2014). Iterative joint inversion for stress and fault orientations from focal mechanisms, *Geophys. J. Int.* **199**, 69–77.
- Waldhauser, F., and W. L. Ellsworth (2000). A double-difference earthquake location algorithm: Method and application to the northern Hayward fault, California, *Bull. Seismol. Soc. Am.* **90**, 1353–1368.
- Wang, M., and Z. K. Shen (2020). Present-day crustal deformation of continental China derived from GPS and its tectonic implications, *J. Geophys. Res.* **125**, no. 2, doi: [10.1029/2019JB018774](https://doi.org/10.1029/2019JB018774).
- Wang, S., Y. Liu, X. Shan, C. Qu, G. Zhang, C. Xie, D. Zhao, X. Fan, J. Hua, S. Liang, et al. (2021). Coseismic surface deformation and slip models of the 2021 M_s 6.4 Yangbi (Yunnan, China) earthquake, *Seismol. Geol.* **43**, 692–705.
- Warren-Smith, E., B. Fry, L. Wallace, E. Chon, S. Henrys, A. Sheehan, K. Mochizuki, S. Schwartz, S. Webb, and S. Lebedev (2019). Episodic stress and fluid pressure cycling in subducting oceanic crust during slow slip, *Nature Geosci.* **12**, 475–481.
- Wegmüller, U., C. Werner, T. Strozzi, A. Wiesmann, O. Frey, and M. Santoro (2016). Sentinel-1 support in the GAMMA software, *Procedia Comput. Sci.* **100**, 1305–1312.
- Xie, Z., S. Li, and Y. Lv (2015). b values spatial distribution characteristics of the main active faults in southwestern Yunnan, *Earth Sci. 10*, 1755–1766 (in Chinese).
- Xu, W. B. (2017). Finite-fault slip model of the 2016 Mw 7.5 Chiloe earthquake, southern Chile, estimated from Sentinel-1 data, *Geophys. Res. Lett.* **44**, 4774–4780.
- Yamashita, F., E. Fukuyama, S. Xu, H. Kawakata, K. Mizoguchi, and S. Takizawa (2021). Two end-member earthquake preparations illuminated by foreshock activity on a meter-scale laboratory fault, *Nat. Commun.* **12**, doi: [10.1038/s41467-021-24625-4](https://doi.org/10.1038/s41467-021-24625-4).
- Yang, T., B. Li, L. Fang, Y. Su, Y. Zhong, J. Yang, M. Qin, and Y. Xu (2021). Relocation of the foreshocks and aftershocks of the 2021 Ms 6.4 Yangbi earthquake sequence, Yunnan, China, *J. Earth Sci.* 1–23, doi: [10.1007/s12583-021-1527-7](https://doi.org/10.1007/s12583-021-1527-7).
- Yao, D., Y. Huang, Z. Peng, and R. R. Castro (2020). Detailed investigation of the foreshock sequence of the 2010 Mw7.2 El Mayor-Cucapah earthquake, *J. Geophys. Res.* **125**, e2019JB019076, doi: [10.1029/2019JB019076](https://doi.org/10.1029/2019JB019076).
- Yoon, C. E., N. Yoshimitsu, W. L. Ellsworth, and G. C. Beroza (2019). Foreshocks and mainshock nucleation of the 1999 Mw 7.1 Hector Mine, California, earthquake, *J. Geophys. Res.* **124**, 1569–1582.
- Zhang, K., W. Gan, S. Liang, G. Xiao, C. Dai, Y. Wang, Z. Li, L. Zhang, and G. Ma (2021). Coseismic displacement and slip distribution of the 2021 May 21, M_s 6.4, Yangbi earthquake derived from GNSS observations, *Chin. J. Geophys.* **64**, no. 7, 2253–2266.
- Zhang, L., S. Liang, X. Yang, and C. Dai (2021). The migration of the crustal deformation peak area in the eastern Himalayan syntaxis inferred from present-day crustal deformation and morpho-tectonic markers, *Geodes. Geodyn.* **12**, 165–174.
- Zhang, Y., Y. An, F. Long, G. Zhu, M. Qin, Y. Zhong, Q. Xu, and H. Yang (2022). Short-term foreshock and aftershock patterns of the 2021 Ms 6.4 Yangbi earthquake sequence, *Seismol. Res. Lett.* **93**, 21–32.
- Zhang, Z., H. Yao, and Y. Yang (2020). Shear wave velocity structure of the crust and upper mantle in southeastern Tibet and its geodynamic implications, *Sci. China Earth Sci.* **63**, 1278–1293.
- Zhao, G., G. Meng, X. Su, W. Wu, Z. Pan, and Q. Zhao (2020). Study on the characteristics of present-day structural deformation and seismic hazard on the southeastern margin of the Qinghai-Tibet plateau, *CGU General Assembly 2020*, Chinese Geoscience Union, CGU, Chongqing, China, 18 October 2020.
- Zhou, Y., A. Ghosh, L. Fang, H. Yue, and S. Zhou (2021). Foreshock sequence of the 2021 Mw6.1 YangBi earthquake sequence, Yunnan, China: Not a triggered cascade, *The 2021 SCEC Annual Meeting*, USA, 12–17 September 2021, available at <https://www.scec.org/meetings/2021/am/poster/226> (last accessed December 2021) (Online).
- Zoback, M. L. (1992). First- and second-order patterns of stress in the lithosphere: The world stress map project, *J. Geophys. Res.* **97**, 11,703–11,728.

Manuscript received 17 September 2021

Published online 30 March 2022